1-1-1991

Numerical Simulation of Electromagnetic Acoustic Transducer in the Time Domain

Reinhold Ludwig
Worcester Polytechnic Institute, ludwig@wpi.edu

X. W. Dai

Numerical simulation of electromagnetic acoustic transducer in the time domain

R. Ludwig and X.-W. Dai
Department of Electrical Engineering, Worcester Polytechnic Institute, Worcester, Massachusetts 01609

(Received 9 July 1990; accepted for publication 6 September 1990)

A novel multistage numerical modeling approach to simulate acoustic-wave generation and propagation of an electromagnetic acoustic transducer (EMAT) is presented. The model assumes a uniform static magnetic field in a conducting half-space. A meander coil winding situated above the half-space is driven by a transient high-frequency current pulse. The numerically computed eddy currents in the conducting specimen are combined with the static magnetic field to yield spatially and temporally diffusive Lorentz forces which in turn are coupled into the elastic-wave equation. This hyperbolic elastodynamic system is solved for the displacement field vector which gives rise to propagating elastic waves. Numerical transduction results are discussed for a generic two-wire transient EMAT configuration and for an isotropic half-space with electric and acoustic material parameters equivalent to those of aluminum.

I. INTRODUCTION

For many nondestructive evaluation (NDE) applications exploiting the propagation and reflection of ultrasonic energy, the direct coupling of conventional piezoelectric transducers to the specimen under test proves to be difficult or even impossible. This is especially true in the steel industry, where surface roughness and elevated temperature of the specimen do not permit intimate coupling of the sensor. In these cases electromagnetic acoustic transducers (EMAT's) are often an ideally suited alternative since they generate bulk or surface elastic waves through electrodynamic principles by typically employing a suspended coil driven by a high-frequency transient current in the presence of a static magnetic field.

In the past, considerable research efforts have been devoted to study the underlying physical principles[1-3] of these electroacoustic sensors for a wide variety of configurations and applications. Most of the analytical treatment to quantify the EMAT transduction phenomena are based on time-harmonic far-field derivations and simplifying assumptions with regard to the underlying constitutive relations arising from the coupling between the elastic and electromagnetic fields, induced field distributions, and elastic-wave generation and propagation mechanisms.

In our model we propose a numerical approach to overcome some of the aforementioned simplifications. In particular, we introduce a unified, self-consistent numerical formulation which encompasses the following discrete steps:

(1) Numerical transient eddy current simulations of a high-frequency excitation coil which is placed between the electromagnet or permanent magnet and the specimen under test in a noncontact mode.

(2) Coupling of the static magnetic field and the induced eddy currents into dynamic Lorentz forces.

(3) Utilization of the Lorentz forces as sources of ultrasonic wave propagation in a transient numerical elastodynamic formulation.

Our numerical model realistically describes transient magnetic field distributions within the solid specimen. Furthermore, the elastic-wave equation is solved for two-dimensional geometries in the time domain without resorting to restrictive far-field assumptions.

The paper is organized as follows: Section II gives a brief review of the physical principles responsible for the electroacoustic generation of ultrasound. Section III then focuses on the numerical implementation of these equations solvable on a workstation-type computer system. In Sec. IV simulation results of eddy current and Lorentz force distributions as well as transient displacement predictions are shown based on a pulsed current excitation.

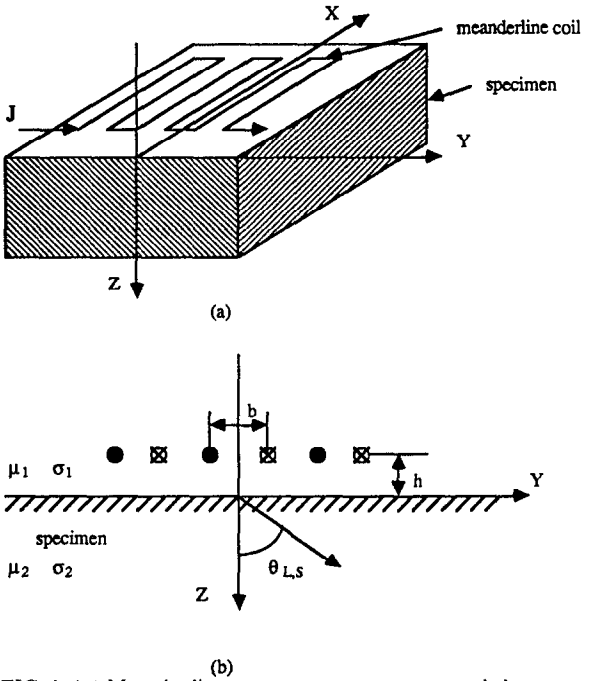

FIG. 1. (a) Meander line current arrangement suspended over conducting specimen. (b) 2D representation of wire placement above solid specimen.

 0021-8979/91/01089

II. THEORETICAL MODEL FORMULATION

The underlying principles of ultrasonic wave generation induced by eddy currents in the presence of a static magnetic field are well understood and documented.[4] Figure 1 depicts a generic two-dimensional EMAT configuration of a meanderline wire coil suspended above a conducting specimen. The excitation loop as well as the metallic specimen are immersed in a static magnetic field which for the purpose of subsequent comparison with analytical studies is assumed to be of uniform flux density B_0 in the y direction, i.e., $\mathbf{B}_0 = B_0 \mathbf{e}_y$, where $\mathbf{e}_y$ is the y-directed unit vector. The field equations governing eddy current phenomena are derived from Ampere's and Faraday's laws:

$$\nabla \times \mathbf{B} = \sigma \mathbf{E} + \mu\epsilon \frac{\partial \mathbf{E}}{\partial t}, \tag{1}$$

$$\nabla \times \mathbf{E} = -\frac{\partial \mathbf{B}}{\partial t}, \tag{2}$$

where $\mathbf{B}$, $\mathbf{E}$, μ, σ, ϵ are, respectively, magnetic flux density, electric field, permeability, conductivity, and permittivity. The magnetic vector potential $\mathbf{A}$ is introduced such that

$$\nabla \times \mathbf{A} = \mathbf{B}$$

and

$$\mathbf{E} = \frac{\partial \mathbf{A}}{\partial t} - \nabla\phi \quad (\phi = \text{scalar potential}).$$

Substitution of the magnetic vector potential into (1) and observing the Lorentz condition

$$\nabla \cdot \mathbf{A} = -\mu\epsilon \frac{\partial \phi}{\partial t}$$

results in the inhomogeneous hyperbolic partial differential equation

$$\nabla^2 \mathbf{A} - \mu\sigma \frac{\partial \mathbf{A}}{\partial t} - \mu\epsilon \frac{\partial^2 \mathbf{A}}{\partial t^2} = \mu\sigma \nabla\phi, \tag{3}$$

where the term $-\sigma\nabla\phi$ is the conduction current $\mathbf{J}$. Since typical current excitation frequencies associated with practical coil arrangements rarely exceed a few MHz, the second time derivative in (3) can be neglected, thus transforming the hyperbolic system into a diffusion equation

$$\nabla^2 \mathbf{A} - \mu\sigma \frac{\partial \mathbf{A}}{\partial t} = -\mu \mathbf{J}. \tag{4}$$

In a 2D, y-z coordinate system, $\mathbf{A}$ and $\mathbf{J}$ have only single vector components A_x, J_x. Thus, (4) can be reexpressed for the geometry of Fig. 1 as a scalar equation:

$$\left(\frac{\partial^2}{\partial y^2} + \frac{\partial^2}{\partial z^2}\right) A_x - \mu\sigma \frac{\partial A_x}{\partial t} = -\mu\delta(z+h) \sum_{k=1}^{N} \{I_{-k}\delta[y - (2k-1)b/2] + I_{+k}\delta[y + (2k-1)b/2]\}, \tag{5}$$

where $\delta(\ )$ indicates the Dirac delta distribution, h is the lift-off distance from the specimen to the wires, and b is the separation between the wires. The transient excitation current $I_{\pm k}(t)$ is assumed to be a raised cosine function (Fig. 2) with

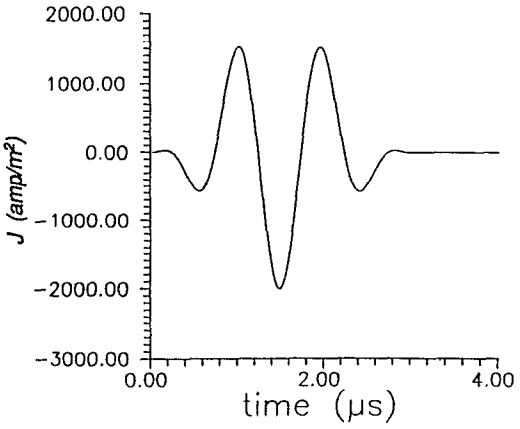

FIG. 2. Transient excitation current based on (6).

$$I_{\pm k}(t) = \begin{cases} \pm(-1)^k I_0 [1 - \cos(\omega_0 t/3)] \cos\omega_0 t \\ \quad \text{for } 0 \leqslant t \leqslant 6\pi/\omega_0, \\ 0 \quad \text{for } t \geqslant 6\pi/\omega_0, \end{cases} \tag{6}$$

where I_0 is a constant current and $\omega_0 = 2\pi f_0$ is the angular center frequency. The boundary conditions along the half-space $z = 0$ (see Fig. 1) are

$$A_{1x}(y, z=0, t) = A_{2x}(y, z=0, t) \tag{7a}$$

and

$$\frac{1}{\mu_1} \frac{\partial A_{1x}}{\partial z}\bigg|_{z=0} = \frac{1}{\mu_2} \frac{\partial A_{2x}}{\partial z}\bigg|_{z=0}. \tag{7b}$$

Here indices 1 and 2 refer to medium 1 for $z < 0$ and medium 2 for $z > 0$. The initial condition on $A_x(y,z,t=0)$ is set to zero.

Upon solving (5) for $A_x(y,z,t)$, the eddy current distribution $\mathbf{J}_e(y,z,t)$ for $z > 0$ is determined by

$$\mathbf{J}_e(y,z,t) = -\sigma \frac{\partial A_x}{\partial t} \mathbf{e}_x. \tag{8}$$

The force mechanisms responsible for the EMAT radiation are based on three major contributions:

$$\mathbf{f} = \nabla \cdot \mathbf{T} + \mathbf{f}_J + \mathbf{f}_M, \tag{9}$$

where $\mathbf{f}_J$ and $\mathbf{f}_M$ are body or volume source densities

$$\mathbf{f}_J(y,z,t) = \mathbf{J}_e(y,z,t) \times \mathbf{B}_0 \tag{10}$$

and

$$\mathbf{f}_M(y,z,t) = \nabla \mathbf{B} \cdot \mathbf{M}. \tag{11}$$

Here $\mathbf{f}_J$ denotes Lorentz forces as a result of the interaction between induced eddy current distribution (8) and the impressed static magnetic field $\mathbf{B}_0$. This force term is always present in a conducting material (magnetic or nonmagnetic). However, in magnetic materials additional magnetization forces $\mathbf{f}_M$ are generated due to the reorientation of magnetic dipoles whose density is denoted by $\mathbf{M}$ in (11). While the body forces are considered long range, there is an additional surface or short-range force mechanism as expressed through the divergence of the second rank stress tensor $\mathbf{T}$ in

(9).[5] This stress tensor in its general form contains two terms:

$$\mathbf{T} = \mathbf{c}:\mathbf{S} - \mathbf{e}\cdot\mathbf{H}, \tag{12}$$

where the first term on the right-hand side is Hooke's law in its linear and anisotropic form with the fourth-rank elastic material tensor $\mathbf{c}$ contracted over the strain tensor $\mathbf{S}$ which in turn is expressed in dyadic displacement notation $\mathbf{u}(y,z,t)$ as

$$\mathbf{S} = \tfrac{1}{2}(\nabla\mathbf{u} + \mathbf{u}\nabla).$$

Furthermore, magnetostriction is accounted for in the term $\mathbf{e}:\mathbf{H}$. The magnetostrictive coefficients entering the third-rank tensor $\mathbf{e}$ are typically determined through measurements.[6]

In the absence of reliable experimental data concerning magnetic dipole density $\mathbf{M}$ and magnetostrictive coefficient tensor $\mathbf{e}$ and in order to avoid complex calculations, force mechanisms due to magnetization and magnetostriction are neglected. This simplification appears reasonable in light of the dominance of the Lorentz forces.[7] The force vector in (9) is therefore approximated by

$$\mathbf{f} = \nabla\cdot(\mathbf{c}:\mathbf{S}) + \mathbf{J}_e\times\mathbf{B}_0. \tag{13}$$

Incorporating (13) into Newton's law

$$\mathbf{f} = \rho\frac{\partial^2\mathbf{u}}{\partial t^2} \tag{14}$$

yields the inhomogeneous elastic-wave equation for anisotropic solids with electrodynamic Lorentz force density. Here ρ is the material density. Reexpressing (13) and (14) in index notation gives

$$c_{ijkl}S_{kl,j} + \epsilon_{ijk}(J_e)_j(B_0)_k = \rho\frac{\partial^2 u_i}{\partial t^2}, \tag{15}$$

where equal indices imply summation and the comma implies differentiation with respect to the following indices. The term ϵ_{ijk} is the third-rank Levi–Civita pseudo tensor.[8] The parentheses are used to separate subscripts from indicial notation. The boundary condition on the surface is assumed to be stress free, i.e., $T_{ij}n_j = 0$. Here n_j are the components of surface normal vector. Subsequent results are discussed based on an isotropic elastic constant tensor whose coefficients are given in terms of the Lamé constants λ,μ, (Ref. 8) (note: μ here is not to be confused with the previously defined electric permeability):

$$c_{ijkl} = \lambda\delta_{ij}\delta_{kl} + \mu(\delta_{ik}\delta_{jl} + \delta_{il}\delta_{jk}), \tag{16}$$

where δ_{ij} denotes the Kronecker delta. Therefore, (15) takes on the form

$$c_L^2\nabla\nabla\cdot\mathbf{u} - c_S^2\nabla\times\nabla\times\mathbf{u} + \rho^{-1}\mathbf{J}_e\times\mathbf{B}_0 = \frac{\partial^2\mathbf{u}}{\partial t^2}, \tag{17}$$

where the longitudinal and shear sound velocities for an isotropic solid are given by

$$c_L^2 = \frac{\lambda+2\mu}{\rho} \quad\text{and}\quad c_S^2 = \frac{\mu}{\rho}. \tag{18}$$

For the following numerical solution approach, (4), (8), and (15) constitute the basic set of equations to be modeled subject to the current input (6).

III. NUMERICAL IMPLEMENTATION

A. Electrodynamic system discretization

The numerical implementation of the EMAT system requires the coupling of the parabolic diffusion equation (4) with the hyperbolic wave equation (15) based on the Lorentz forces (10). A convenient way of solving these coupled equations is by means of a weighted residual approach. This technique in the context of eddy current phenomena is discussed in detail by several authors,[9–11] and only a brief description is given. The starting point is the formulation of an inner product between (4) and polynomial weighting functions ϕ_i, with i denoting interpolation nodes within the solution domain Ω

$$\left\langle\left(\nabla^2 A_x - \mu\sigma\frac{\partial A_x}{\partial t} + \mu J_x\right)\phi_i\right\rangle = 0, \tag{19}$$

where $\langle\ \rangle$ indicates integration of the domain Ω. Integration by parts and subsequent approximation of A_x, J_x by Galerkin-type trial functions[12]

$$A_x \cong \sum_j A_{xj}\phi_j \quad\text{and}\quad J_x \cong \sum_j J_{xj}\phi_j \tag{20}$$

results in

$$\left\langle\frac{\partial\phi_j}{\partial y}\frac{\partial\phi_i}{\partial y} + \frac{\partial\phi_j}{\partial z}\frac{\partial\phi_i}{\partial z}\right\rangle A_{xj} + \langle\mu\sigma\phi_j\phi_i\rangle\frac{dA_{xj}}{dt} - \langle\mu\phi_j\phi_i\rangle J_{xj} = \int_L\frac{\partial A_x}{\partial n}\phi_i\,dL, \tag{21}$$

where the line integral along L accounts for the Neumann-type boundary condition and where n is the outwards pointing normal. (21) can be expressed more concisely in matrix notation:

$$[S]\{A_x\} + [C]\{\dot{A}_x\} - [D]\{J_x\} = \{Q_x\}. \tag{22}$$

Here the matrices $[S]$, $[C]$, $[D]$ represent the assembled integral contributions of (21) over the total number of nodes in Ω. The column vectors $\{A_x\}$, $\{\dot{A}_x\}$, $\{J_x\}$, and $\{Q_x\}$ contain the total nodal contributions of the magnetic vector potential, its time derivative, current density, and Neumann boundary conditions. A transient, time-stepping algorithm is achieved by introducing in (22) a backward difference formula:

$$\{\dot{A}_x\}_{t+\Delta t} \cong (1/\Delta t)(\{A_x\}_{t+\Delta t} - \{A_x\}_t), \tag{23}$$

with Δt being the step size. Thus, the system to be evaluated takes on the form[13,14]

$$\left([S] + \frac{1}{\Delta t}[C]\right)\{A_x\}_{t+\Delta t} = \frac{1}{\Delta t}[C]\{A_x\}_t + [D]\{J_x\}_{t+\Delta t} + \{Q_x\}_{t+\Delta t}. \tag{24}$$

Simulating a causal system initially at rest, the condition $\{A_x\}_0$ is set to zero. The evaluation of (24) can be carried out by standard linear algebra techniques of inverting a banded linear matrix at each time step.[15] The eddy currents in the specimen in conjunction with a uniform field $\mathbf{B}_0$ yield the desired Lorentz force distribution directed along the z-axis:

$$\{f_z\}_{t+\Delta t} = -(\sigma B_0/\Delta t)(\{A_x\}_{t+\Delta t} - \{A_x\}_t). \tag{25}$$

Equation (25) can now be used as source term in the discretized form of (17) as discussed in the next section.

B. Acoustic system discretization

Similar to the electrodynamic derivation (17), the weighted residual approach can again be employed to discretize (15). Therefore, the starting point is[16]

$$\langle (T_{\alpha\beta,\beta} + f_\alpha - \rho u_{\alpha,tt})\phi_i \rangle = 0, \tag{26}$$

with Greek indices indicating the two spatial Cartesian coordinates y,z. Integrating by parts yields

$$\langle T_{\alpha\beta}\phi_{i,\beta} \rangle - \langle f_\alpha \phi_i \rangle + \langle \rho u_{\alpha,tt}\phi_i \rangle = \int_L T_{\alpha\beta} n_\beta \phi_i \, dL. \tag{27}$$

Rewriting (27) in matrix notation and substitution of isotropic elastic coefficients

$$\left\langle \begin{bmatrix} \phi_{i,y} & 0 & \phi_{i,z} \\ 0 & \phi_{i,z} & \phi_{i,y} \end{bmatrix} \begin{bmatrix} \lambda+2\mu & \lambda & 0 \\ \lambda & \lambda+2\mu & 0 \\ 0 & 0 & \mu \end{bmatrix} \begin{bmatrix} \frac{\partial}{\partial y} & 0 \\ 0 & \frac{\partial}{\partial z} \\ \frac{\partial}{\partial z} & \frac{\partial}{\partial y} \end{bmatrix} \begin{Bmatrix} u_y \\ u_z \end{Bmatrix} \right\rangle - \left\langle \begin{bmatrix} \phi_i & 0 \\ 0 & \phi_i \end{bmatrix} \begin{Bmatrix} f_y \\ f_z \end{Bmatrix} \right\rangle + \left\langle \rho \begin{bmatrix} \phi_i & 0 \\ 0 & \phi_i \end{bmatrix} \begin{Bmatrix} u_{y,tt} \\ u_{z,tt} \end{Bmatrix} \right\rangle = \begin{Bmatrix} \int T_{y\beta} n_\beta \phi_i \, dl \\ \int T_{z\beta} n_\beta \phi_i \, dl \end{Bmatrix}. \tag{28}$$

Inserting polynomial expansion functions for the displacement field **u** and Lorentz force density **f**,

$$u_\alpha \cong \sum_j u_{\alpha j}\phi_j \quad \text{and} \quad f_\alpha \cong \sum_j f_{\alpha j}\phi_j, \tag{29}$$

leads to

$$\left\langle \begin{bmatrix} \phi_{i,y} & 0 & \phi_{i,z} \\ 0 & \phi_{i,z} & \phi_{i,y} \end{bmatrix} \begin{bmatrix} \lambda+2\mu & \lambda & 0 \\ \lambda & \lambda+2\mu & 0 \\ 0 & 0 & \mu \end{bmatrix} \times \begin{bmatrix} \phi_{j,y} & 0 \\ 0 & \phi_{j,z} \\ \phi_{j,z} & \phi_{j,y} \end{bmatrix} \right\rangle \begin{Bmatrix} u_{yj} \\ u_{zj} \end{Bmatrix} - \left\langle \begin{bmatrix} \phi_i\phi_j & 0 \\ 0 & \phi_i\phi_j \end{bmatrix} \right\rangle \begin{Bmatrix} f_{yj} \\ f_{zj} \end{Bmatrix} + \left\langle \rho \begin{bmatrix} \phi_i\phi_j & 0 \\ 0 & \phi_i\phi_j \end{bmatrix} \right\rangle \begin{Bmatrix} u_{yj,tt} \\ u_{zj,tt} \end{Bmatrix} = \begin{Bmatrix} \int T_{y\beta} n_\beta \phi_i \, dl \\ \int T_{z\beta} n_\beta \phi_i \, dl \end{Bmatrix}. \tag{30}$$

Equation (30) can be written in more compact form as

$$[K]\{u_\alpha\} - [M]\{f_\alpha\} + \rho[M]\{\ddot{u}_\alpha\} = \{Q_\alpha\}, \tag{31}$$

where the column vectors are global quantities for displacement vector $\{u_\alpha\}$, force density $\{f_\alpha\}$, and acceleration $\{\ddot{u}_\alpha\}$. The index α denotes two displacement field components or degrees of freedom for each individual node in the solution domain Ω. The coefficients of the matrices $[K]$ and $[M]$ and the right-hand side $\{Q_\alpha\}$ are[17]

$$K_{ij} = \langle \mathbf{b}_i^{\mathrm{T}} \mathbf{c} \mathbf{b}_j \rangle, \tag{32a}$$

$$M_{ij} = \langle \mathbf{b}_i^{\mathrm{T}} \mathbf{b}_j \rangle, \tag{32b}$$

$$Q_{\alpha i} = \int T_{\alpha\beta} n_\beta \phi_i \, dL, \tag{32c}$$

with the constitutive terms in (32a) and (32b) defined as

$$\mathbf{b}_j = \begin{bmatrix} \phi_{j,y} & 0 \\ 0 & \phi_{j,z} \\ \phi_{j,z} & \phi_{j,y} \end{bmatrix}, \tag{33a}$$

$$\mathbf{c} = \begin{bmatrix} \lambda+2\mu & \lambda & 0 \\ \lambda & \lambda+2\mu & 0 \\ 0 & 0 & \mu \end{bmatrix}. \tag{33b}$$

As can be seen from (33b), the discretized version (31) of the elastic-wave equation is capable of handling anisotropic materials if the elastic constants in (33b) are changed to more general terms. Moreover, **c** can spatially vary throughout Ω, thus accounting for nonuniform material parameters.

C. Computational Implementation

System (31) can be solved in the time domain in various ways.[18,19] In anticipation of solving a very large system of equations, an explicit method with lumping of the $[M]$ matrix[20] is chosen. The advantage of such a method is complete elimination of matrix inversion, thus allowing efficient computations on workstation-type (Hewlett-Packard HP 9000 series 835) computers. In order to achieve this task, a central difference approximation for the second time derivative in (31) is selected:

$$\{\ddot{u}_\alpha\}_t = (1/\Delta t^2)(\{u_\alpha\}_{t+\Delta t} - 2\{u_\alpha\}_t + \{u_\alpha\}_{t-\Delta t}). \tag{34}$$

Substituting into (31) and rearranging terms results in

$$\{u_\alpha\}_{t+\Delta t} = \frac{\Delta t^2}{\rho}[M]^{-1}(\{Q_\alpha\}_t - [K]\{u_\alpha\}_t) + \frac{\Delta t^2}{\rho}\{f_\alpha\}_t + 2\{u_\alpha\}_t - \{u_\alpha\}_{t-\Delta t}. \quad (35)$$

The inversion of $[M]$ is facilitated by first diagonalizing the matrix according to[21]

$$M_{ii}^{\text{diag}} = M_{ii}\left(\sum_j \sum_k M_{jk} \Big/ \sum_j M_{jj}\right), \quad (36)$$

followed by scaling the diagonalized matrix elements

$$[M]^{-1} \cong [1/M_{ii}^{\text{diag}}]. \quad (37)$$

Therefore, (35) can be computed without resorting to the computer-time-consuming matrix inversion at each time step. The algorithm is started by specifying the first two displacement vectors $\{u_\alpha\}_0$ and $\{u_\alpha\}_{-\Delta t}$ as part of the initial condition.

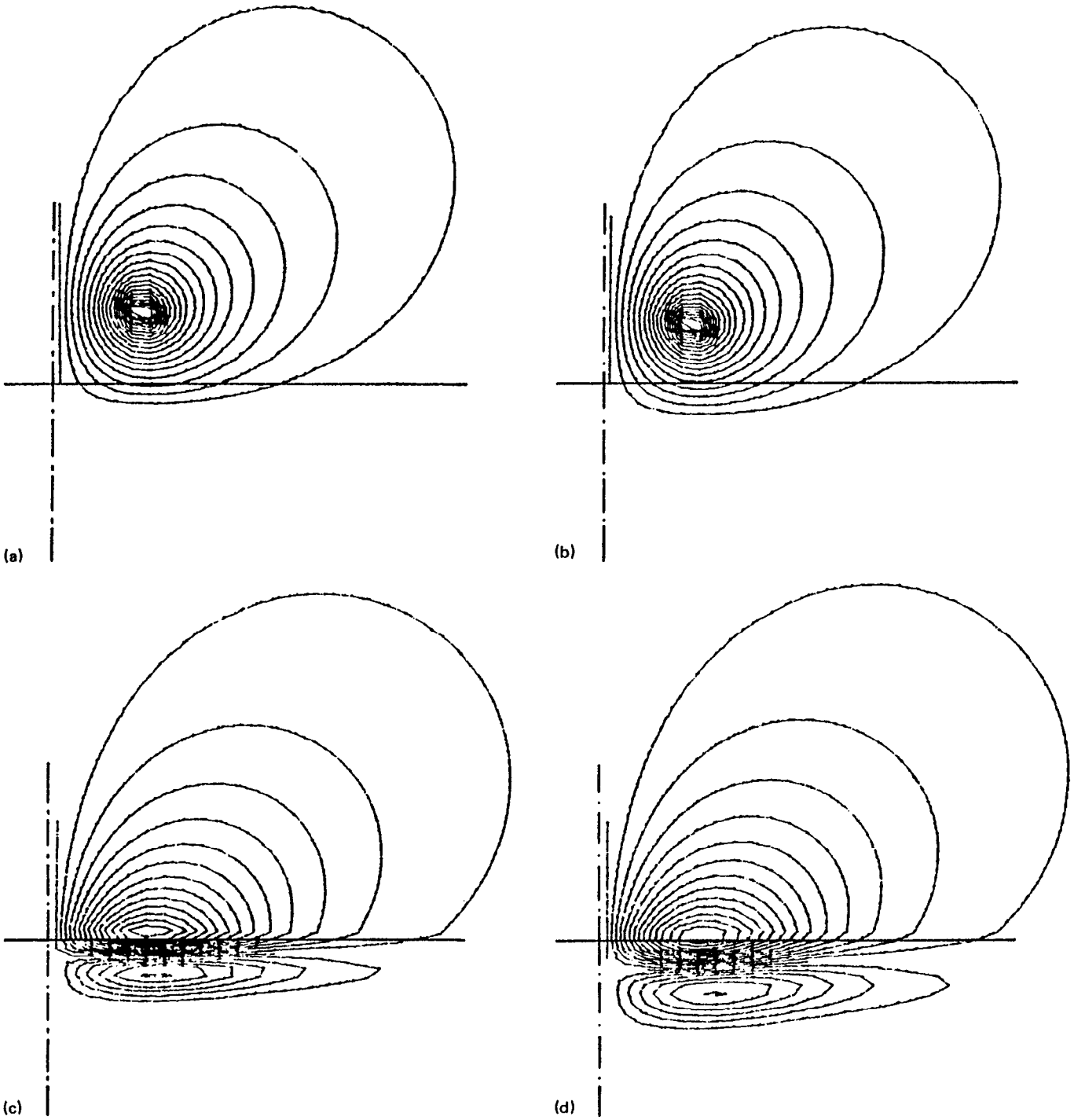

FIG. 3. Magnetic vector potential distribution for (a) $t = 0.5\,\mu$s, (b) $t = 2.5\,\mu$s, (c) $t = 4.5\,\mu$s, and (d) $t = 6.5\,\mu$s. Note: due to symmetry about the z axis, only half a plane is shown.

IV. NUMERICAL PREDICTIONS

A. Generic EMAT arrangement

In order to test the previously outlined model formulation and its numerical implementation, a two-wire coil configuration is simulated. Consequently, the parameters in (5) are specified as $N = 1$, $h = 1$ mm, and $b = 2$ mm. The specimen is assumed to be nonmagnetic, $\mu = \mu_0$, with a conductivity of $\sigma = 3.5 \times 10^7$ S/m. In (6) the pulsed current has a frequency f_0 of 1 MHz and I_0 is 1000 A. In addition, the specimen is immersed in a constant magnetic field of $B_0 = 1$ T. For more practically relevant cases involving realistic electromagnets or permanent magnets, an existing numerical analysis package[22] could be employed to compute the nonuniform flux densities in the specimen under test. The acoustical properties of the specimen are those of aluminum with Lamé constants λ, μ of 2.76×10^{10} and 5.19×10^{10} N/m^2 and a density of $\rho = 2700$ kg/m^3. The longitudinal and shear sound velocities c_L and c_S according to (18) are therefore 6.3 and 3.2 mm/μs.

The numerical results reported in the following section are based on separate spatial discretizations for the electrodynamic and elastodynamic model. In particular, due to the limited depth of penetration of the magnetic field, a smaller electrodynamic mesh is chosen. The magnetic vector potential is computed with a spatial resolution of $\Delta y = \Delta z = 0.1$ mm, resulting in a total number of 16 200 triangular elements and dimensions of 10 mm in the z direction and 20 mm in the y direction. The time step size for the implicit algorithm (24) and the Lorentz force density (25) is chosen to be $\Delta t = 10$ ns. The electrodynamic simulation typically requires the computation of 500 time steps. In contrast, the elastodynamic equation of motion is discretized into $\Delta y = \Delta z = 0.2$ mm and $\Delta t = 10$ ns. These numbers amount to 32 nodes per longitudinal and 16 nodes per shear wavelength. The total number of quadrilateral elements is 360 000, resulting in dimensions of 120 mm in both z and y directions. For the reported displacement predictions typically 1800 time steps need to be computed. Despite the large number of elements, the explicit algorithm (35) can be efficiently solved on a workstation with at least 25 MBytes of main memory.

B. Numerical field predictions

Based on the aforementioned system parameters, the field quantities for the electro- and elastodynamic equations are computed. In Fig. 3 the single component magnetic vector potential as a solution of (24) is shown for different instances in time as a function of space. The vector potential is then coupled through (25) to produce the z-directed Lorentz force density. Figure 4 shows the temporal distribution of the Lorentz force density on the surface of the specimen directly underneath the respective wire. As expected, the time history of the force density follows the current excitation as specified in Fig. 2. However, due to the diffusive nature of the eddy currents, the Lorentz forces develop a volumetric expansion. This effect is demonstrated in Fig. 5 for two instances in time. As can be seen, the force distribution is antisymmetric because of the opposite polarity of the driving current in the wire. Furthermore, the field magnitude diminishes rapidly for locations below the surface.

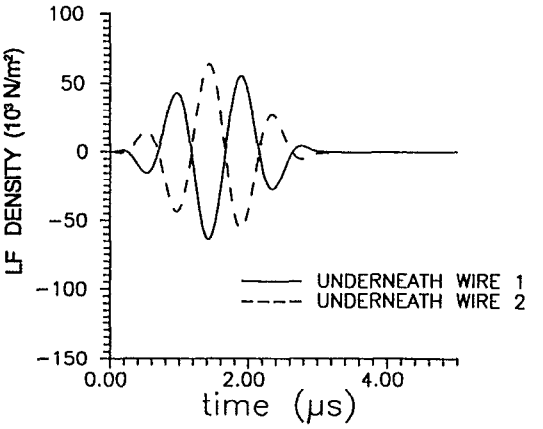

FIG. 4. Temporal Lorentz force distribution on the surface ($z = 0$) for $y = -b/2$ (wire 1) and $y = +b/2$ (wire 2).

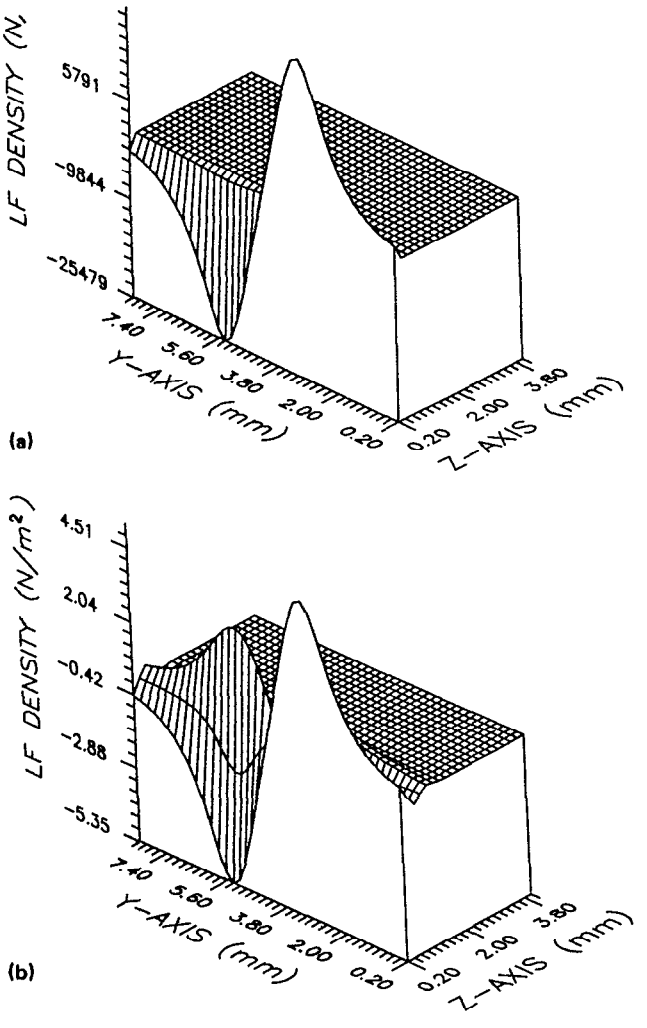

FIG. 5. Spatial Lorentz force distribution in the half-space at (a) $t = 1.0\,\mu$s and (b) $t = 5\,\mu$s.

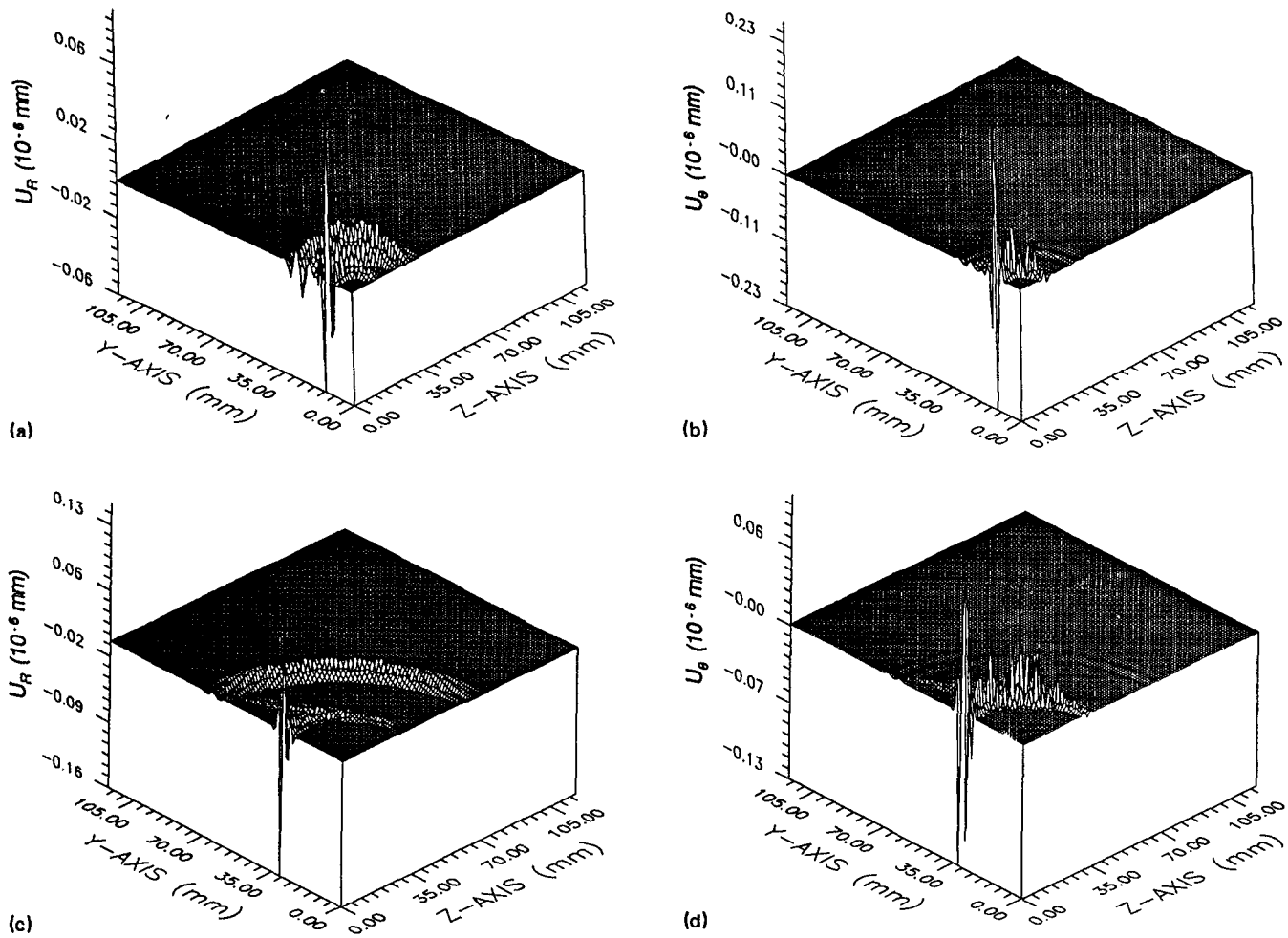

FIG. 6. Displacement field for wire spacing $b = 2$ mm. (a) Radial component u_R and (b) tangential component u_θ, both at $t = 6$ μs, and (c) radial component u_R and (d) tangential component u_θ, both at $t = 12$ μs.

The computed spatial and temporal force densities can now be employed as input function $\{f_\alpha\}_t$ in the discrete elastodynamic representation of the acoustic-wave equation (31). The resulting transient radial and tangential displacement field predictions, u_R and u_θ, are shown in Fig. 6. Due to the symmetry about the z axis, only half a plane is computed. The spatial field distribution for the time instances 6 and 12 μs reveal the emanating longitudinal and shear bulk waves. On the surface, the shear wave front becomes a surface wave. In addition, in order to satisfy the stress-free boundary conditions, a head wave connecting both wave fronts can be identified. Alternatively, by defining a spatial

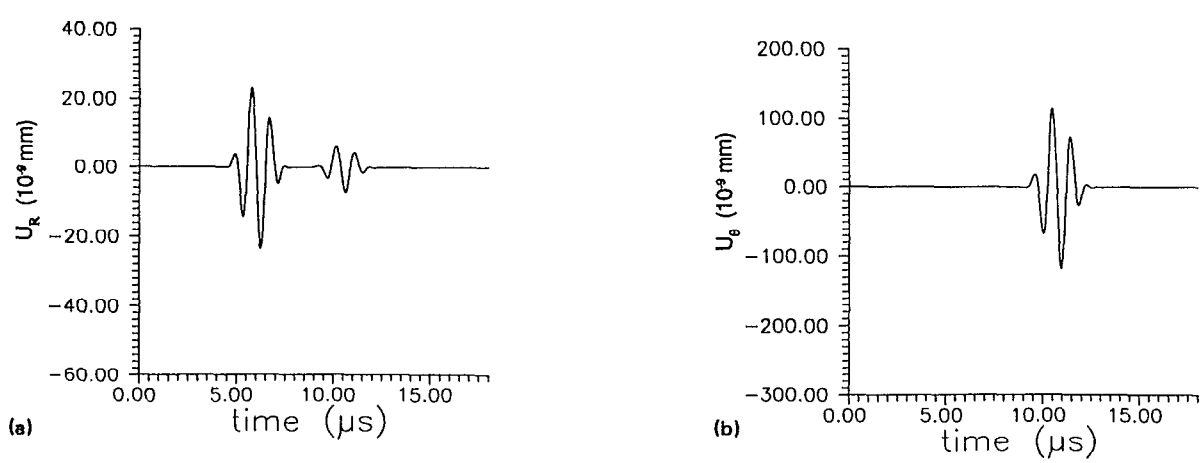

FIG. 7. Displacement field response based on $b = 2$ mm wire spacing and spatial location $y = 20$ mm and $z = 20$ mm for (a) u_R and (b) u_θ components.

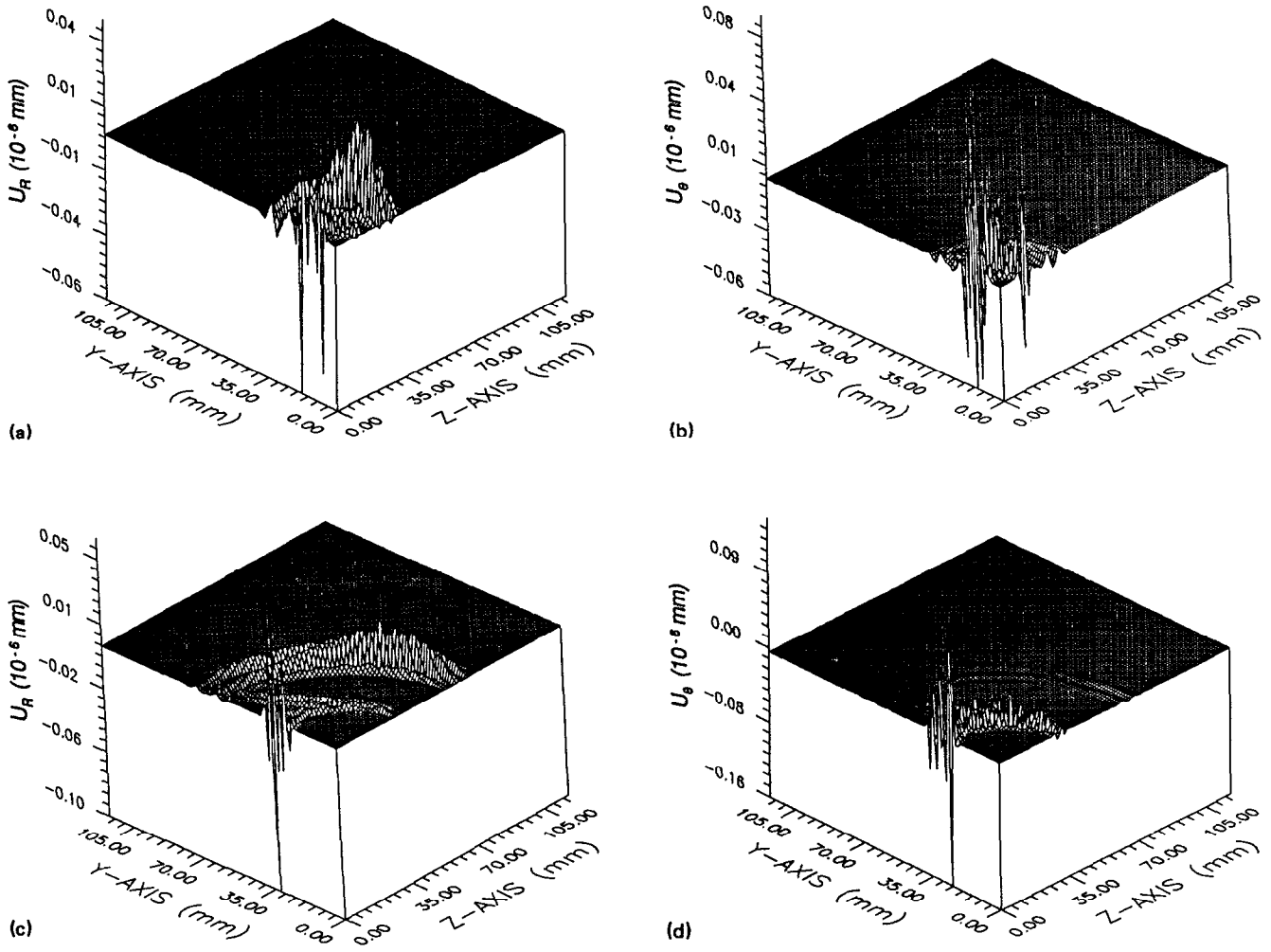

FIG. 8. Displacement field for wire spacing $b = 6.2$ mm. (a) Radial component u_R and tangential component u_θ, both at $t = 6\,\mu$s, and (c) radial component u_R and (d) tangential component u_θ, both at $t = 12\,\mu$s.

coordinate point and recording increments in time, the time-amplitude (A-scan) response for this point is found. Figure 7 depicts the u_R and u_θ components for location $z = 20$ mm and $y = 20$ mm in the half-space. It is evident that the u_θ component is approximately five times larger in amplitude than the u_R component.

In contrast, Fig. 8 shows the transient spatial displacement response for the same instances in time as in Fig. 6 but for a wire spacing of $b = 6.2$ mm. The resulting time-amplitude displacement response corresponding to Fig. 7 is given in Fig. 9. A comparison between Figs. 7 and 9 indicate a widening of the ultrasonic pulses for an increase in wire sepa-

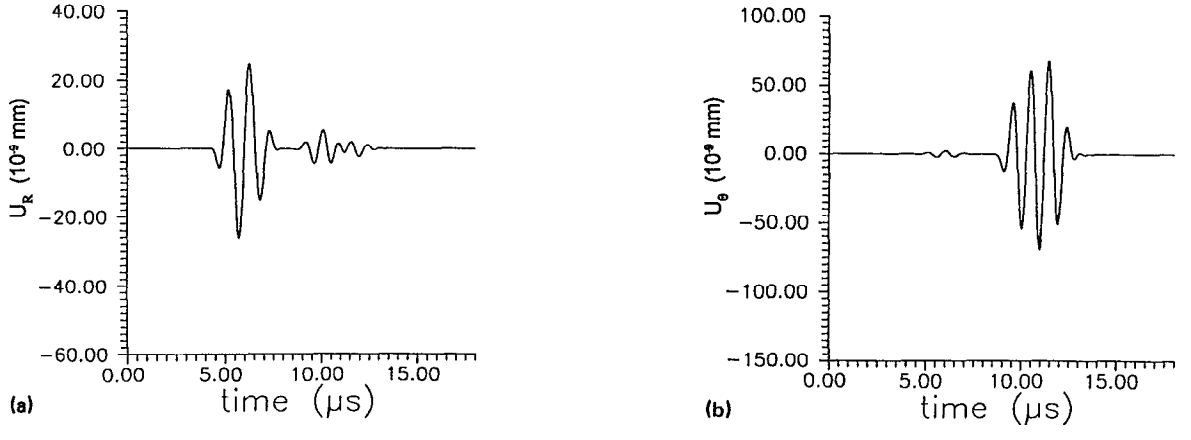

FIG. 9. Displacement field response based on $b = 6.2$ mm wire spacing and spatial location $y = 20$ mm and $z = 20$ mm for (a) u_R and (b) u_θ components.

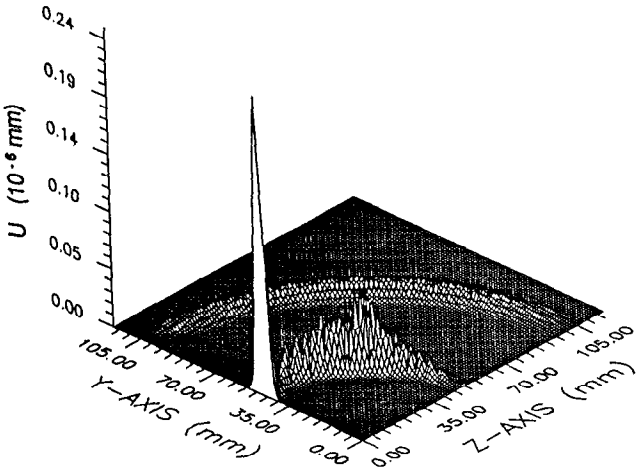

FIG. 10. Magnitude of composite displacement field U for $b = 2$ mm and at $t = 18\ \mu$s.

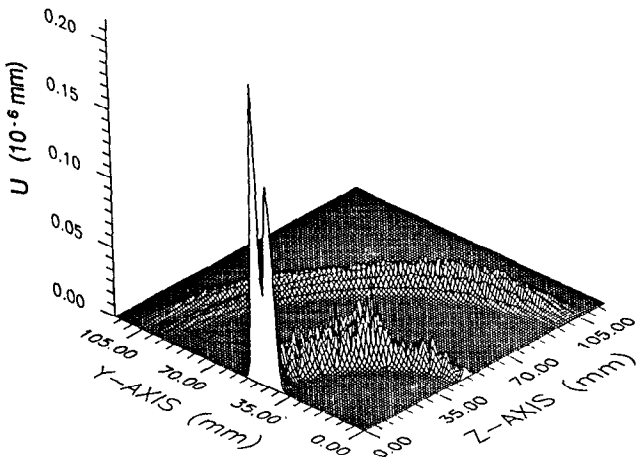

FIG. 11. Magnitude of composite displacement field U for $b = 6.2$ mm and at $t = 18\ \mu$s.

ration. Furthermore, unlike Fig. 7, the u_θ component is only twice as large in amplitude compared with the u_R component.

The radiation angle of the bulk wave fields can be approximately compared with the analytical expression for isotropic solids[23]:

$$\theta_{L,S} = \sin^{-1}(Nc_{L,S}/2f_0 b), \tag{38}$$

where $N = 1$, $c_L = 6300$ m/s, $c_S = 3200$ m/s, and $f_0 = 1$ MHz. It should be pointed out that (38) is derived from Huygens' principle of discrete point radiators situated on the surface of the solid directly underneath the current-carrying wires. Therefore, (38) offers only limited applicability as a plane-wave expression for time-harmonic fields. Nonetheless, if the numerical wave field predictions are recorded sufficiently far away from the source, (38) serves as a good measure of comparison.

Based on a wire spacing of $b = 2$ mm, (38) predicts a shear angle of $\theta_S = 50.8°$. Because θ_L is imaginary, the longitudinal-wave front is evanescent. This fact is also supported by the ratio of the temporal displacement component predictions in Fig. 7 as well as the spatial composite magnitude prediction $U = (u_R^2 + u_\theta^2)^{1/2}$, Fig. 10, indicating in both cases that the shear-wave front carries the main energy with its bulk amplitude maximum located at 48°. In contrast, Fig. 11 shows the simulated composite displacement field for a wire spacing of $b = 6.2$ mm. Here a stronger longitudinal-wave front is predicted which is also reflected in the ratio of the displacement responses as shown in Fig. 9. The corresponding angles based on (37) are now $\theta_L = 29.5°$ and $\theta_S = 14.5°$ and compare with the numerical predictions of approximately $\theta_L = 30°$ and $\theta_S = 45°$. Although the θ_L comparison is in relatively good agreement, the θ_S angle exhibits a rather large discrepancy. This appears to be partially the result of the proximity of the shear-wave fronts to the source, making a clear comparison of amplitude variations for this time instance practically impossible to identify.

V. CONCLUSIONS

In this paper a novel, coupled numerical model in the time domain is presented which permits the quantitative two-dimensional simulation of the EMAT transduction phenomenon. The ability to incorporate spatially and temporally expanding Lorentz force densities as a result of the transient eddy current modeling allows a realistic description of the excitation mechanisms governing the elastic-wave generation and propagation.

Although simulation results are given for an isotropic nonferromagnetic half-space, this modeling approach is general enough to be extended to anisotropic, conducting, and ferromagnetic linear media of complex geometric shapes. Furthermore, by generalizing the force mechanisms responsible for the EMAT radiation, additional terms such as magnetization and magnetostriction could be included in this formulation.

More work remains to be done in studying the precise influence of such variables as excitation coil arrangement, material parameters, and electric excitation mechanisms. However, this present numerical modeling approach clearly shows the potential usefulness both in gaining detailed theoretical insight into the transduction mechanisms and as a tool for practical EMAT designs.

ACKNOWLEDGMENT

This project is supported by the Nondestructive Evaluation (NDE) and Sensor Technology Department, Timken Research, The Timken Company, Canton OH 44706.

[1] W. J. Pardee and R. B. Thompson, J. Nondestruct. Eval. **1**, 157 (1980).
[2] R. B. Thompson, IEEE Trans. Sonics Ultrason. **20**, 340 (1973).
[3] R. B. Thompson, J. Appl. Phys. **48**, 4942 (1977).
[4] H. M. Frost, in *Physical Acoustics*, edited by W. P. Mason (Academic, New York, 1979), Vol. 14, pp. 179–275.
[5] B. A. Auld, *Acoustic Fields and Waves in Solids* (Wiley, New York, 1973), Vol. 1.
[6] A. Wilbrand, in *New Procedures in Nondestructive Testing*, edited by P. Höller (Springer, Berlin, 1983), pp. 71–80.
[7] R. B. Thompson (unpublished).

[8] J. D. Achenbach, *Wave Propagation in Elastic Solids* (North-Holland, Amsterdam, 1973).
[9] W. Lord, IEEE Trans. Magn. **19**, 2437 (1983).
[10] A. J. Butler, Ph.D. dissertation, Department of Electrical Engineering, Carnegie-Mellon University, Pittsburgh, PA, 1990.
[11] C. F. Bryant, C. R. I. Emson, and C. W. Trowbridge, IEEE Trans. Magn. **26**, 430 (1990).
[13] R. Ludwig and X.-W. Dai, IEEE Trans. Magn. **26**, **1**, 299 (1990).
[14] X.-W. Dai, R. Ludwig, and R. Palanisamy, IEEE Trans. Magn. **26**, **6**, 3086 (1990).
[15] W. H. Press, B. P. Flannery, S. A. Teukolsky, and W. T. Vetterling, *Numerical Recipes in Fortran* (Cambridge University Press, Cambridge, England, 1989).
[16] R. Ludwig, D. Moore, and W. Lord, IEEE Trans. Ultrason. Ferroelectr. Freq. Control, **36**, 342 (1989).
[18] M. B. Allen, I. Herrera, and G. F. Pinder, *Numerical Modeling in Science and Engineering* (Wiley, New York, 1988).
[19] T. H. J. Hughes, *The Finite Element Method* (Prentice Hall, Englewood Cliffs, NJ, 1987).
[20] E. Hinton, T. Rock, and O. C. Zienkiewicz, Earthquake Engi. Structural Dynami. **4**, 245 (1976).
[21] D. Moore, R. Ludwig, and W. Lord, Proc. Rev. Progr. Quant. Nondestruct. Eval. **8A**, 103 (1989).
[22] R. Palanisamy, "MAGSTAT, Magnetostatic Finite Element Program," Electric Power Research Report, Project *S* 125-1, Palo Alto, CA, Oct. 1981.
[23] G. A. Alers and L. R. Burns, Mater. Eval. **45**, 1184 (1987).